

**Electronic Supplementary Material (ESI) for Journal of Materials Chemistry A.**

**This journal is © The Royal Society of Chemistry 2019**

## **Supporting Information**

**Biomass-derived hierarchically porous carbon skeletons with *in situ* decorated IrCo nanoparticles as high-performance cathode catalysts for Li–O<sub>2</sub> batteries**

Junrong Shen,<sup>a1</sup> Haitao Wu,<sup>a1</sup> Wang Sun,<sup>\*ab</sup> Qibing Wu,<sup>b</sup> Shuying Zhen,<sup>c</sup> Zhenhua Wang<sup>ad</sup> and Kening Sun<sup>\*ad</sup>

*<sup>a</sup> Beijing Key Laboratory for Chemical Power Source and Green Catalysis, School of Chemistry and Chemical Engineering, Beijing Institute of Technology, Beijing 100081, China*

*<sup>b</sup> State Key Laboratory of Advanced Chemical Power Sources, Guizhou Meiling Power Sources Co. Ltd., Zunyi, Guizhou 563003, China*

*<sup>c</sup> Institute of Advanced Structure Technology, Beijing Institute of Technology, Beijing 100081, China*

*<sup>d</sup> Collaborative Innovation Center of Electric Vehicles in Beijing, No. 5 Zhongguancun South Avenue, Haidian District, Beijing 100081, China*

**<sup>1</sup> These authors contributed equally to this work.**

**\* Corresponding Authors**

\* E-mail: sunwang@bit.edu.cn (Wang Sun); bitkeningsun@163.com (Kening Sun).

## **Experimental Section**

### ***Materials***

Water-soluble starch, iridium chloride hydrate ( $\text{IrCl}_3 \cdot x\text{H}_2\text{O}$ ), cobaltous nitrate hexahydrate ( $\text{Co}(\text{NO}_3)_2 \cdot 6\text{H}_2\text{O}$ ), sodium borohydride ( $\text{NaBH}_4$ ), hydrochloric acid (HCl),  $\text{IrO}_2$ , commercial Ir/C, and  $\text{RuO}_2$  were purchased from Aladdin. Hydrophilic nano- $\text{CaCO}_3$  (~40 nm) powders were purchased from Shanxi Xintai NanoMater Co. Ltd., Pt/C (20 wt.%) was bought from Alfa Aesar. Ultrapure water with a resistivity of 18.25  $\text{M}\Omega \text{ cm}$  was prepared in laboratory. All raw materials were used as received without additional treatment.

### ***Preparation of hierarchical porous carbon skeleton***

First, commercial nano- $\text{CaCO}_3$  (1.0 g) and water-soluble starch (1.0 g) powders were uniformly dispersed in ultrapure water (150 mL). The mixture was freeze-dried and then carbonized at 800 °C for 2 h under argon atmosphere. The carbonized composite was etched with HCl aqueous solution (1 M) for 10 h to remove nano- $\text{CaCO}_3$  templates. Finally, HPCS was obtained after washing with ultrapure water and absolute ethanol followed by overnight vacuum drying at 60 °C.

### ***Preparation of Ir@HPCS and IrCo@HPCS catalysts***

$\text{IrCl}_3 \cdot x\text{H}_2\text{O}$  (16 mg) and  $\text{Co}(\text{NO}_3)_2 \cdot 6\text{H}_2\text{O}$  (13 mg) were added in ultrapure water (25 mL) to obtain a homogeneous solution. Then HPCS (20 mg) was added and the contents were sonicated for 1 h. Subsequently,  $\text{NaBH}_4$  aqueous solution (25 mL, 1 M) was added into the mixture and continuously stirred for 12 h at room temperature. The resulting solution was centrifuged and washed with ultrapure water and absolute

ethanol followed by vacuum drying at 60 °C for 12 h to get the IrCo@HPCS composite. Ir@HPCS was prepared following the same route, but without the addition of  $\text{Co}(\text{NO}_3)_2 \cdot 6\text{H}_2\text{O}$  in the precursor solution.

### ***Characterization***

The morphologies of as-synthesized materials were observed by scanning electron microscopy (SEM, FEI Quanta FEG 250). The microstructures were observed by transmission electron microscopy (TEM, JEOL 2100F). The element distributions and contents were observed by high angle annular dark field scanning transmission electron microscopy (HAADF-STEM, JEOL 2010F) with energy dispersive X-ray spectroscopy (EDS) attachment performed at 200 kV. Metal contents in as-synthesized catalysts were calculated by inductively coupled plasma mass spectrometry (ICP-MS, iCAPQ, Thermo, Waltham, USA). The X-ray diffraction (XRD) was obtained by a Rigaku Ultima IV diffractometer with  $\text{CuK}\alpha$  radiation. Raman characterization was conducted using a Renishaw RM2000 via a 633 nm laser. The  $\text{N}_2$  adsorption/desorption isotherms were obtained by a Quantachrome ASIQM0VH002-5 instrument. The metallic content was estimated by thermogravimetric analysis (TGA, Q5000). The chemical compositions were detected by X-ray photoelectron spectroscopy (XPS, Thermo Fisher K-Alpha).

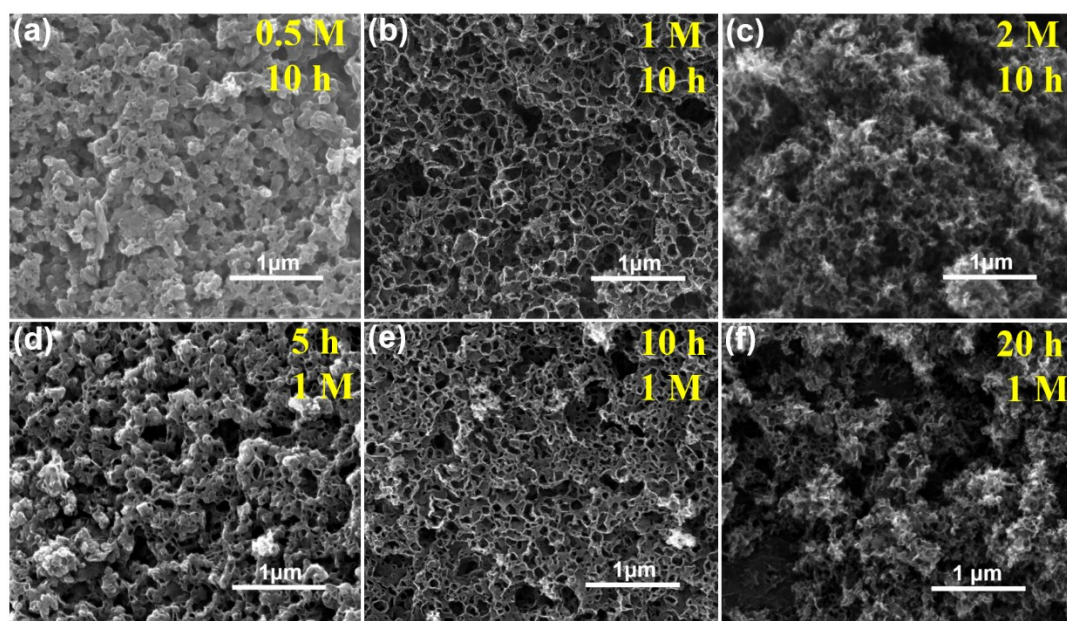
### ***Electrochemical Measurements***

Catalytic activity of catalysts in KOH aqueous solution (0.1 M) was evaluated by a standard three-electrode system with a glassy carbon (GC) rotating disc electrode (RDE,  $0.247 \text{ cm}^2$ ) covered with active materials as working electrode, a Pt wire as

counter electrode, and a mercuric oxide electrode (Hg/HgO) as reference electrode. A homogeneous catalyst ink consisting of the catalyst (2 mg), ethanol (985  $\mu\text{L}$ ), and Nafion (15  $\mu\text{L}$ , 5 wt.%, DuPont) was prepared, and the ink (20  $\mu\text{L}$ ) was dropped onto the GC electrode. For comparison, the purchased Pt/C (20 wt.% Pt), IrO<sub>2</sub>, commercial Ir/C, and RuO<sub>2</sub> catalysts were also tested by the same procedure. All measurements were conducted on a CHI760E electrochemical working station (Chenhua, Shanghai) with a scan speed of 10 mV s<sup>-1</sup>. During the ORR tests, O<sub>2</sub> was continuously flowed over the O<sub>2</sub>-saturated electrolyte and operated at -0.8 to 0.3 V (vs. Hg/HgO). The OER measurements were carried out from 0 to 1.2 V (vs. Hg/HgO) at 1600 rpm. All potentials were compensated by iR and converted into standard hydrogen electrode potential ( $E_{\text{RHE}} = E_{\text{Hg/HgO}} + 0.098 + 0.059\text{pH}$ ).

The electrochemical performance of as-synthesized catalysts in LOBs was measured using the CR2025 coin-type cell with 17 uniformly distributed holes (1 mm diameter) on the cathode side to allow oxygen entry. The air electrode was prepared by spraying mixed slurry, consisting of 90 wt.% catalysts and 10 wt.% polyvinylidene fluoride binder dispersed in *N*-methyl pyrrolidone, onto a carbon paper, which was followed by vacuum drying at 100 °C for 24 h. The total loading density of the catalyst was about 0.35 mg cm<sup>-2</sup>. The current density and specific capacity were normalized to the total mass of the catalyst. Then the air cathode and lithium metal anode were packaged together in an Ar-filled glove box and separated by LiClO<sub>4</sub>/DMSO (1 M) electrolyte-soaked glass fiber separator. For comparison, within 2.2–4.4 V at 500 and 1000 mA g<sup>-1</sup>, 1 M lithium bistrifluoromethanesulfonimide

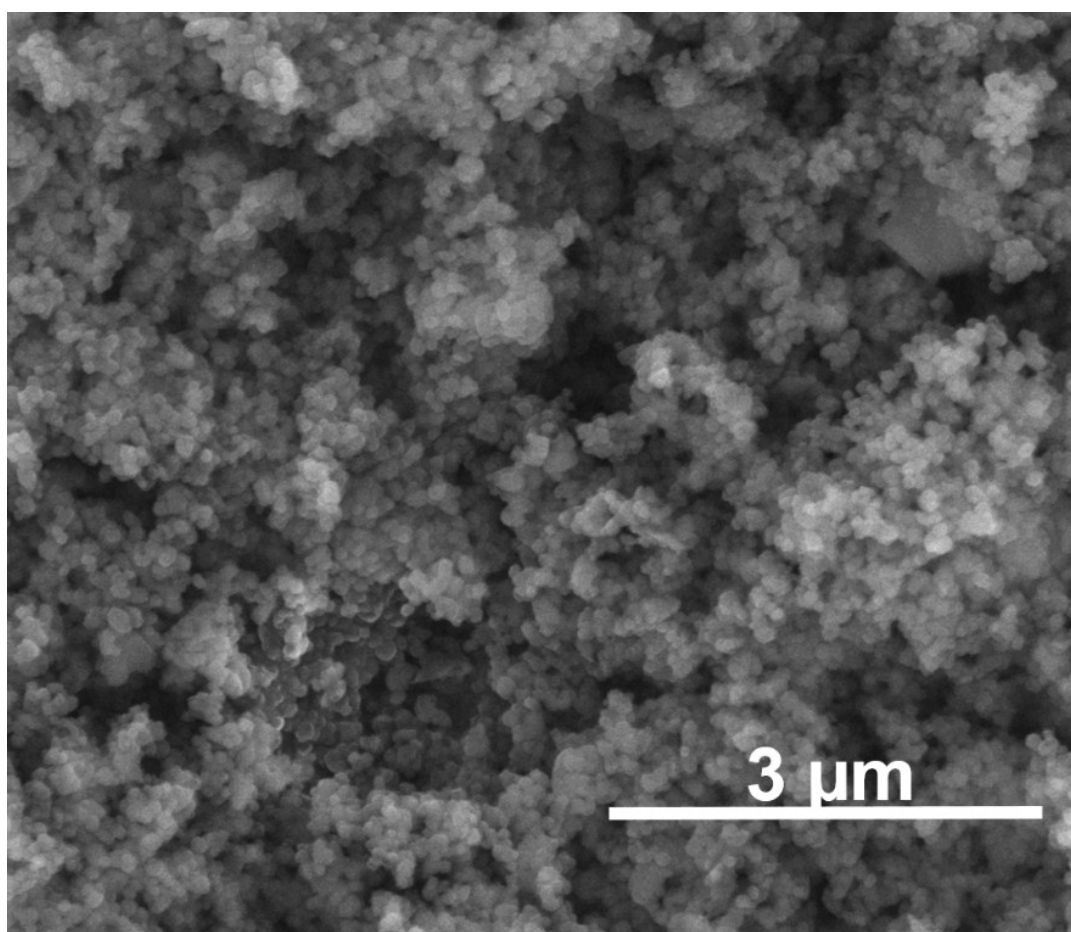
(LiTFSI)/tetraethylene glycol dimethyl ether (TEGDME) electrolyte was also used to verify the catalytic performance of as-prepared catalysts. All galvanostatic discharge/charge measurements were conducted by a LAND battery testing station (CT2001A) under pure oxygen environment.



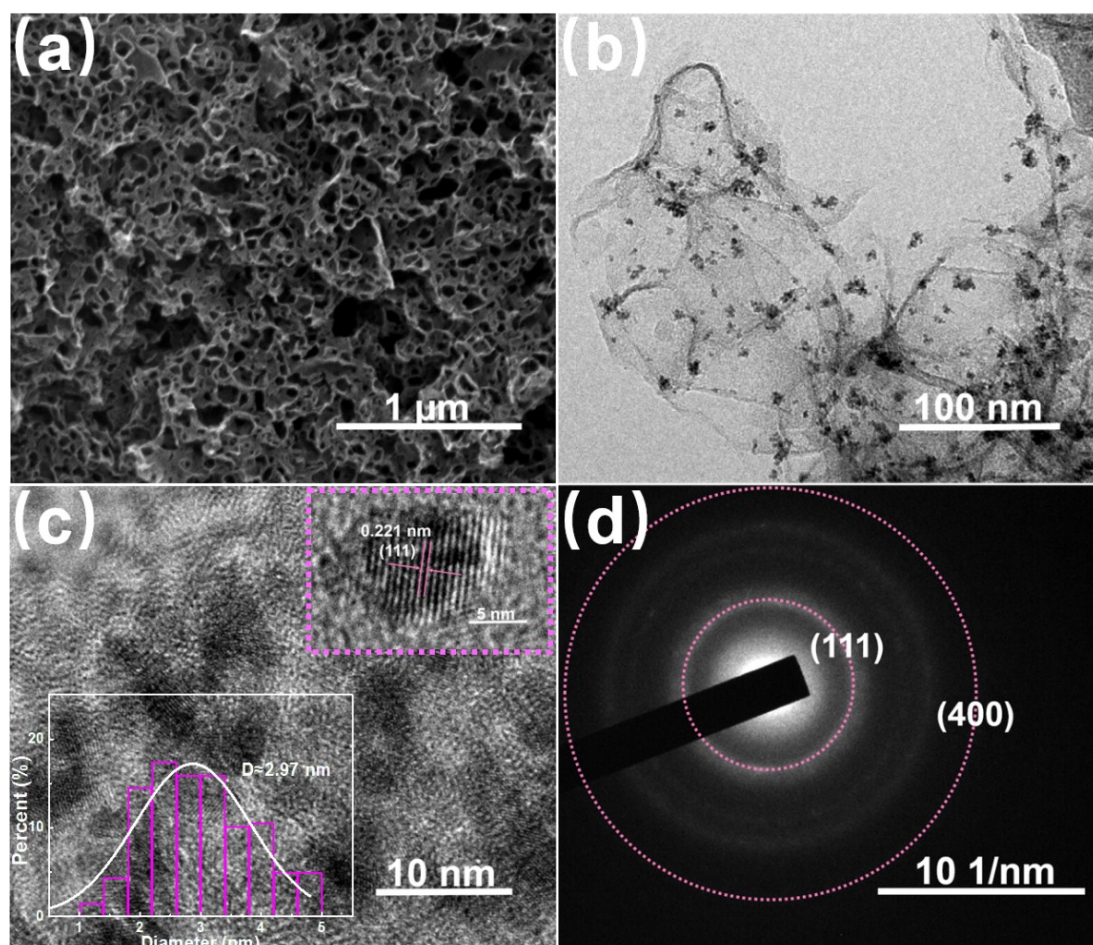
**Fig. S1.** SEM images of HPCS under different etching conditions: (a–c) different HCl concentration and (d–f) different etching time.

Fig. S1a–c shows the effect of different acid concentration on the carbon skeleton morphology at a given etching time (10 h). Fig. S1a shows that the  $\text{CaCO}_3$  template could not be completely removed when etched by 0.5 M HCl for 10 h due to the incomplete acid-base neutralization. While, the proper acid concentration (1 M HCl) would be contributed to form uniquely 3D interconnected porous structure (Fig. S1b). However, when HCl concentration increased to 2 M, the 3D cross-linked skeleton with substantial continuous mesoporous and macroporous channels was severely

damaged (Fig. S1c). This is because a large number of rapidly generated gases ( $\text{CaCO}_3 + 2\text{HCl} = \text{CO}_2\uparrow + \text{CaCl}_2 + \text{H}_2\text{O}$ ) rush out from the interior, resulting in structural fragmentation. Moreover, the etching time also matters the porous structure, as shown in Fig. S1d–f. The nano- $\text{CaCO}_3$  couldn't be effectively removed when etched by 1 M HCl for 5 h because of insufficient reaction time. When etched for 10 h (Fig. S1e), the desired morphology was achieved. However, when extending time from 10 to 20 h (Fig. S1f), the 3D skeleton was destroyed due to the long mechanical stirring. Thus, the proper HCl concentration (1 M) and etching time (10 h) would be contributed to form moderate porous structure and perfect 3D cross-linked skeleton.



**Fig. S2** SEM image of nano- $\text{CaCO}_3$ .



**Fig. S3** (a) SEM and (b) TEM images of Ir@HPCS. (c) High-resolution TEM image of Ir@HPCS.

The insets are corresponding diameter distribution histogram (bottom left) and lattice-resolved TEM image (top right) of Ir nanoparticles. (d) The SAED pattern of Ir@HPCS.

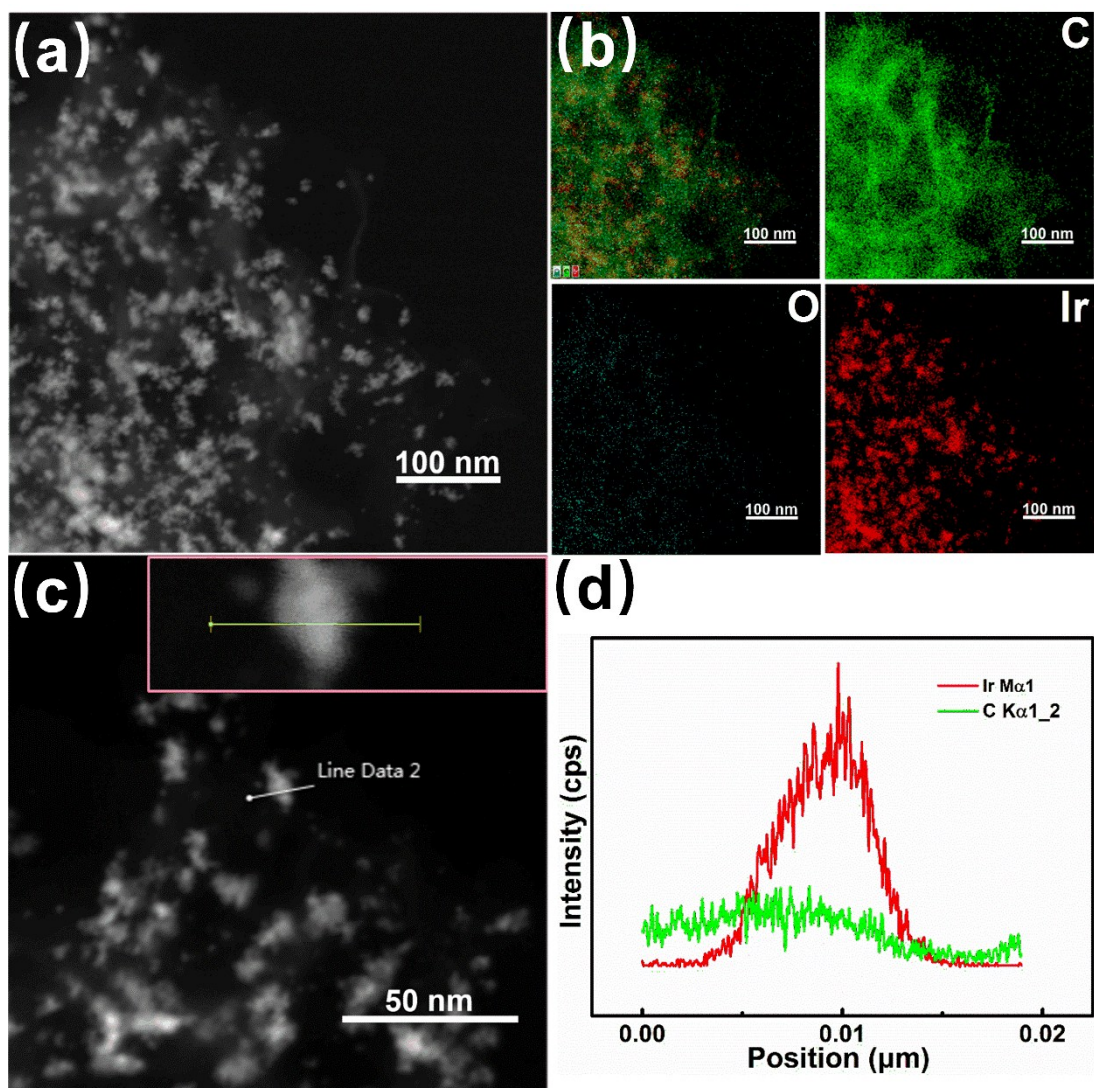


**Fig. S4** (a) HAADF-STEM image and (b) corresponding elemental mappings of Ir@HPCS. (c, d)

Lines scan of an Ir nanoparticle in Ir@HPCS.

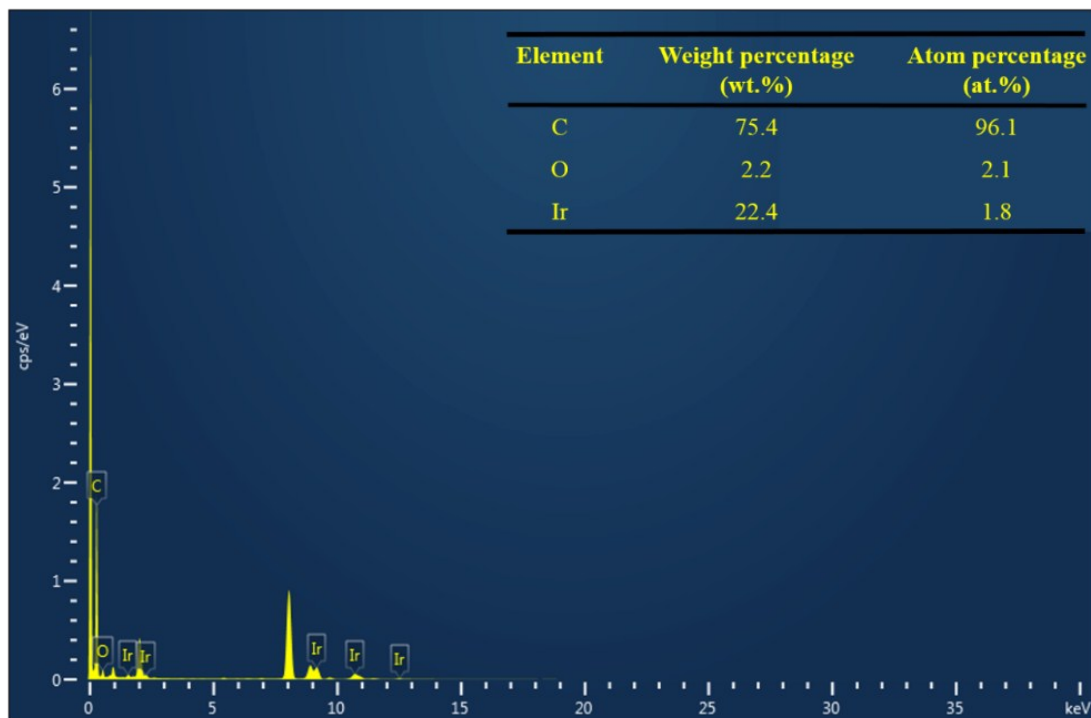


**Fig. S5** Energy dispersive X-ray spectra (EDS) of Ir@HPCS.

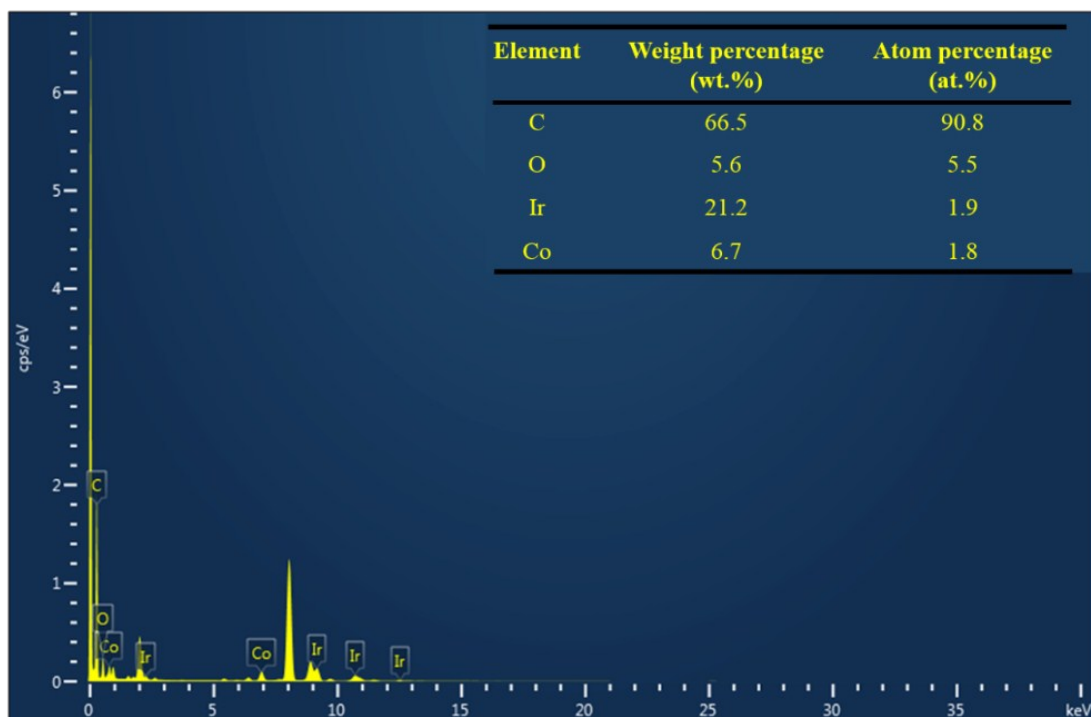


**Fig. S6** EDS of IrCo@HPCS.

**Table S1.** ICP-MS results of Ir@HPCS and IrCo@HPCS.

Catalysts	Content of Ir (wt.%)	Content of Co (wt.%)
Ir@HPCS	23.4	—
IrCo@HPCS	22.8	6.6

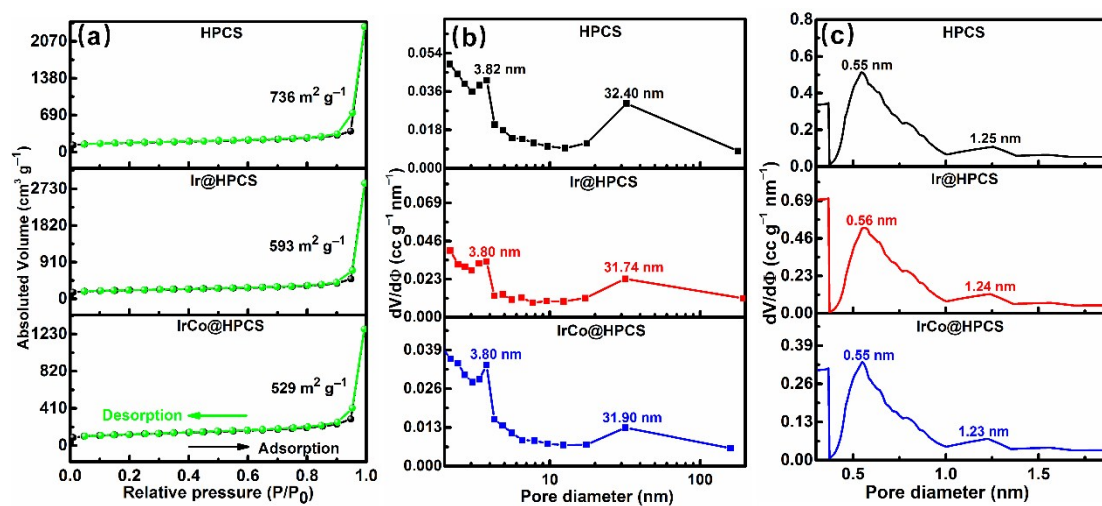


**Fig. S7** (a) The N<sub>2</sub>-adsorption/desorption isotherms of HPCS, Ir@HPCS, and IrCo@HPCS materials. Pore size distributions of HPCS, Ir@HPCS, and IrCo@HPCS materials obtained by (b) BJH (Barrette–Joyner–Halenda) method for mesopores and (c) HK (Horvath–Kawazoe) method for micropores.

**Table S2.** Textural properties of the HPCS, Ir@HPCS, and IrCo@HPCS catalysts.

Catalysts	Specific surface area (m <sup>2</sup> g <sup>-1</sup> )	Micropore size (nm)	Mesopore size (nm)	Total Pore volume (cm <sup>3</sup> g <sup>-1</sup> )
HPCS	736	0.55, 1.25	3.82, 32.40	4.531
Ir@HPCS	593	0.56, 1.24	3.80, 31.74	3.423
IrCo@HPCS	529	0.55, 1.23	3.80, 31.90	2.063

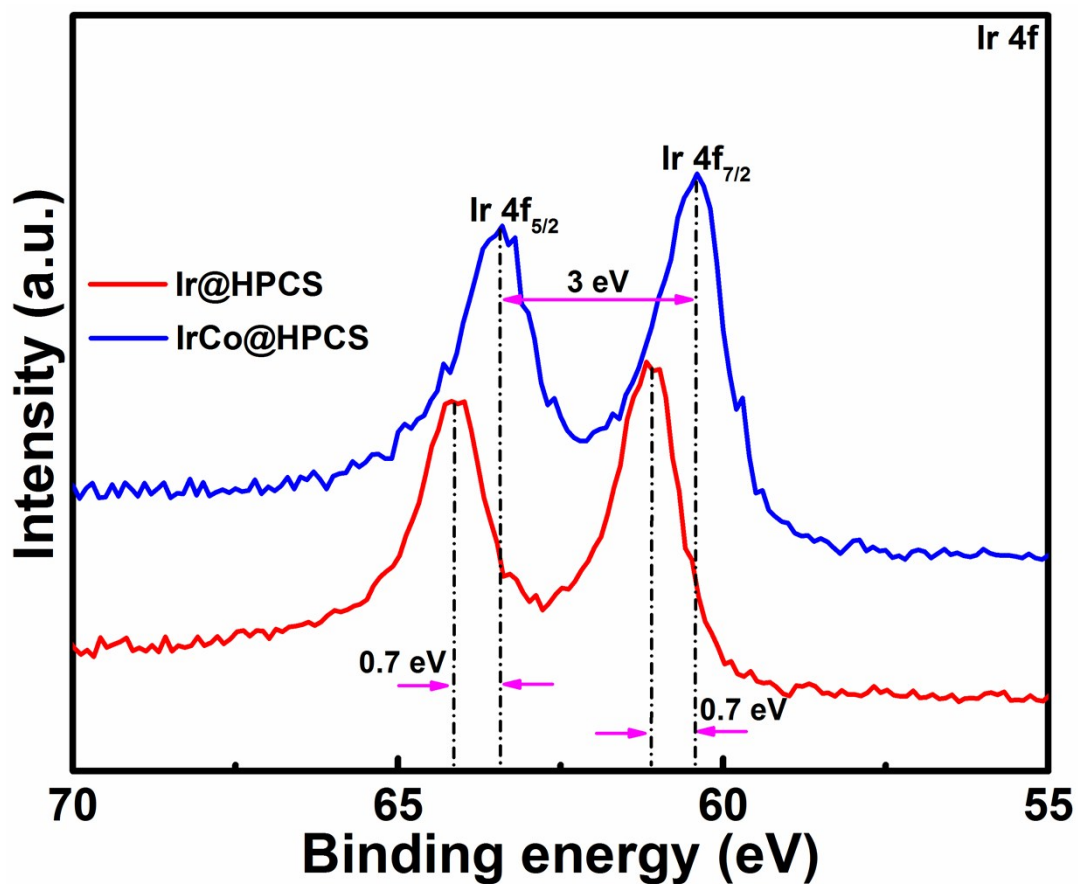
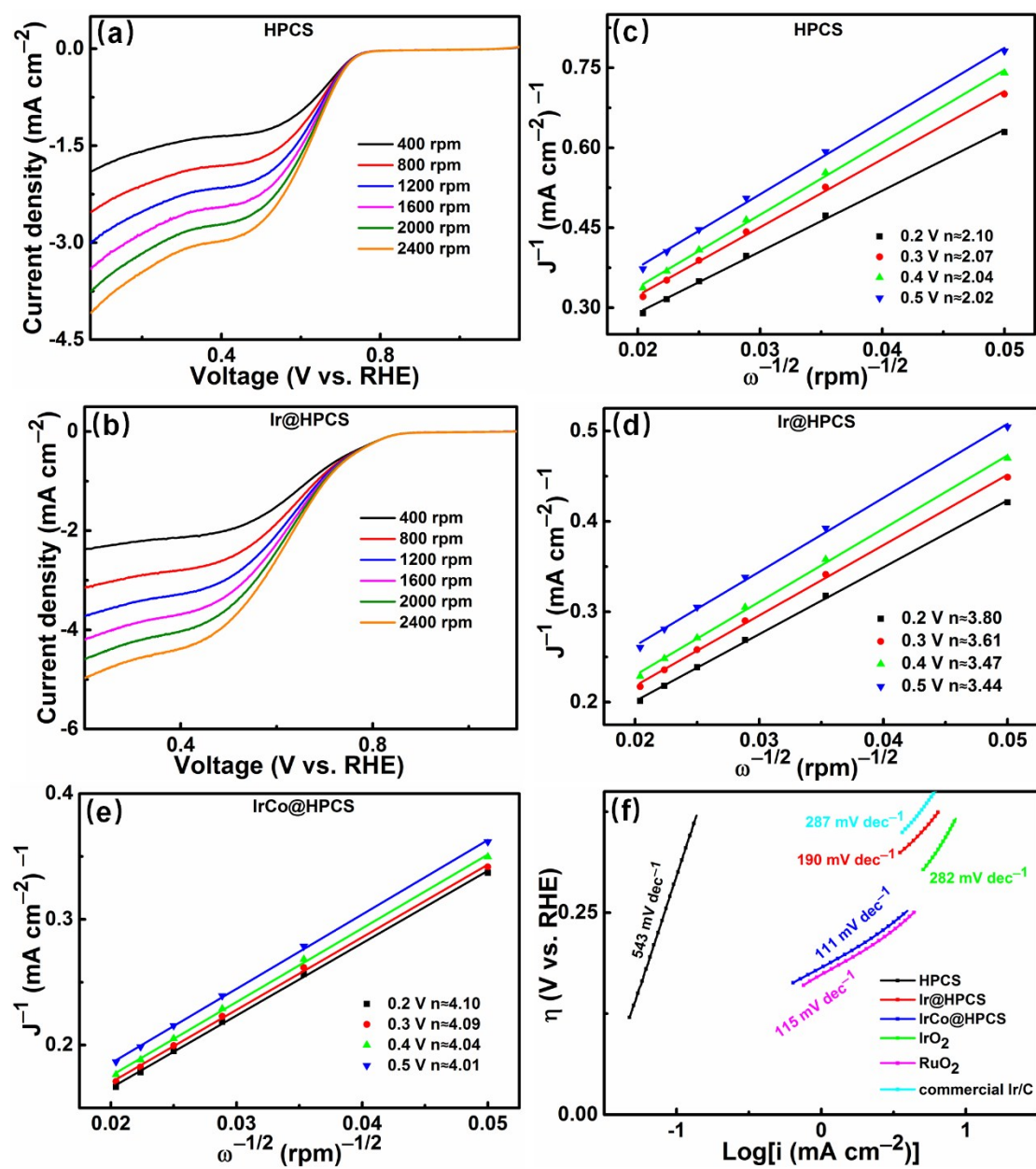


Fig. S8 Ir 4f XPS spectra of Ir@HPCS and IrCo@HPCS.

**Table S3.** The atom ratios of Ir(0) and Ir(IV) in Ir@HPCS and IrCo@HPCS based on XPS results.

Catalysts	Ir(0) peak area (%)	Ir(IV) peak area (%)	Ir(0)/ Ir(IV)
Ir@HPCS	79.7	20.3	3.93
IrCo@HPCS	79.8	20.2	3.95



**Fig. S9** LSV curves of ORR for (a) HPCS and (b) Ir@HPCS. The corresponding K-L plots of (c) HPCS, (d) Ir@HPCS, and (e) IrCo@HPCS. (f) The corresponding OER tafel plots.

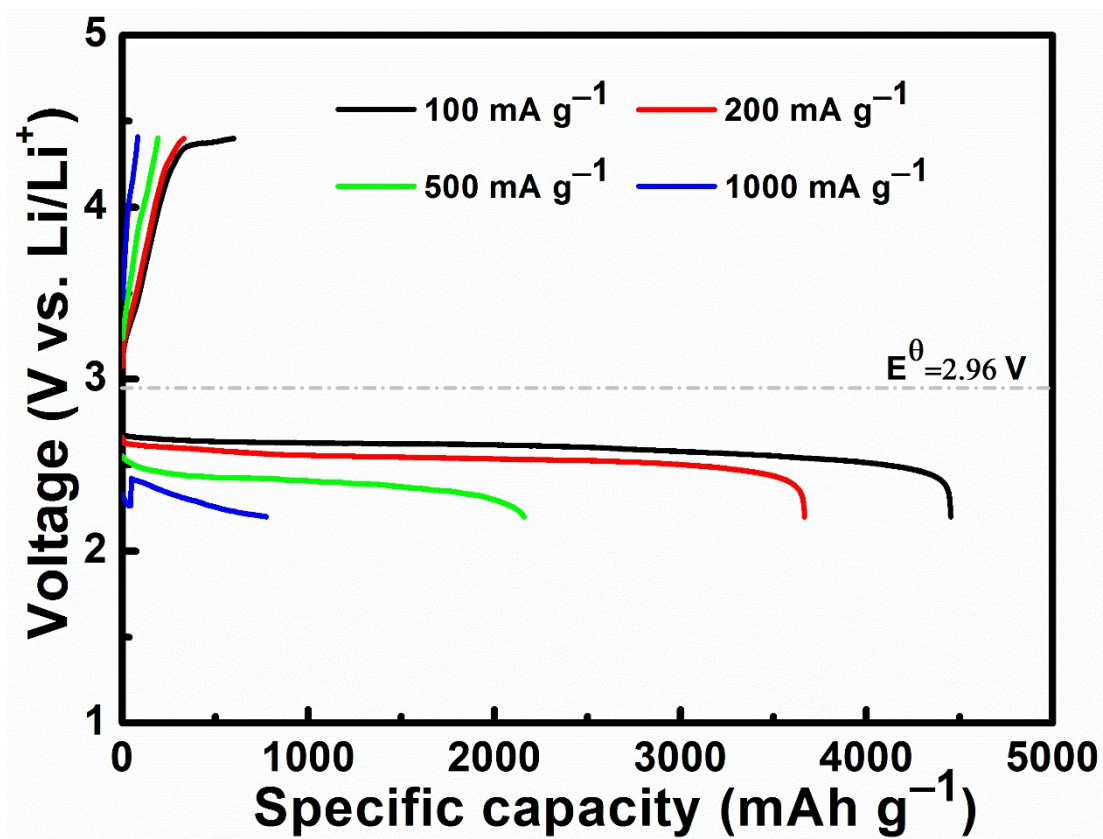


Fig. S10 The rate performance of LOBs with commercial Super P cathodes.

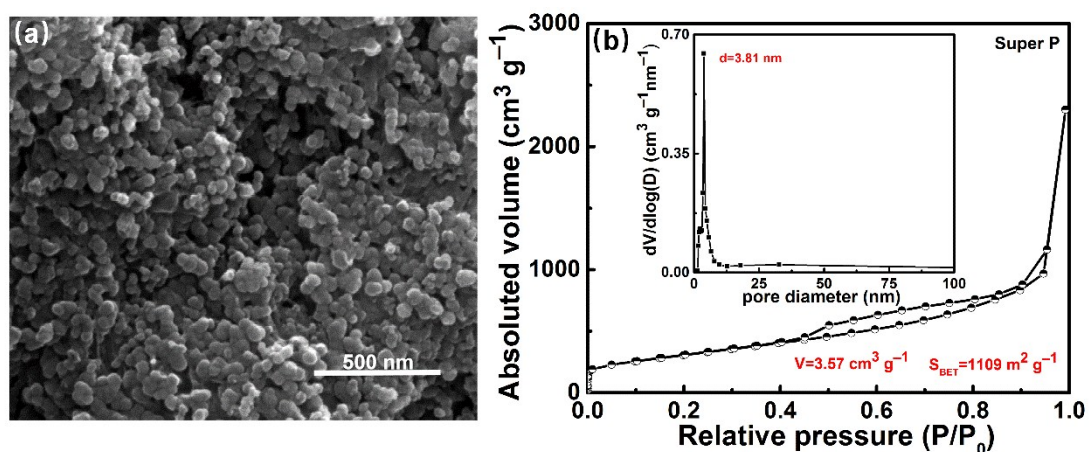
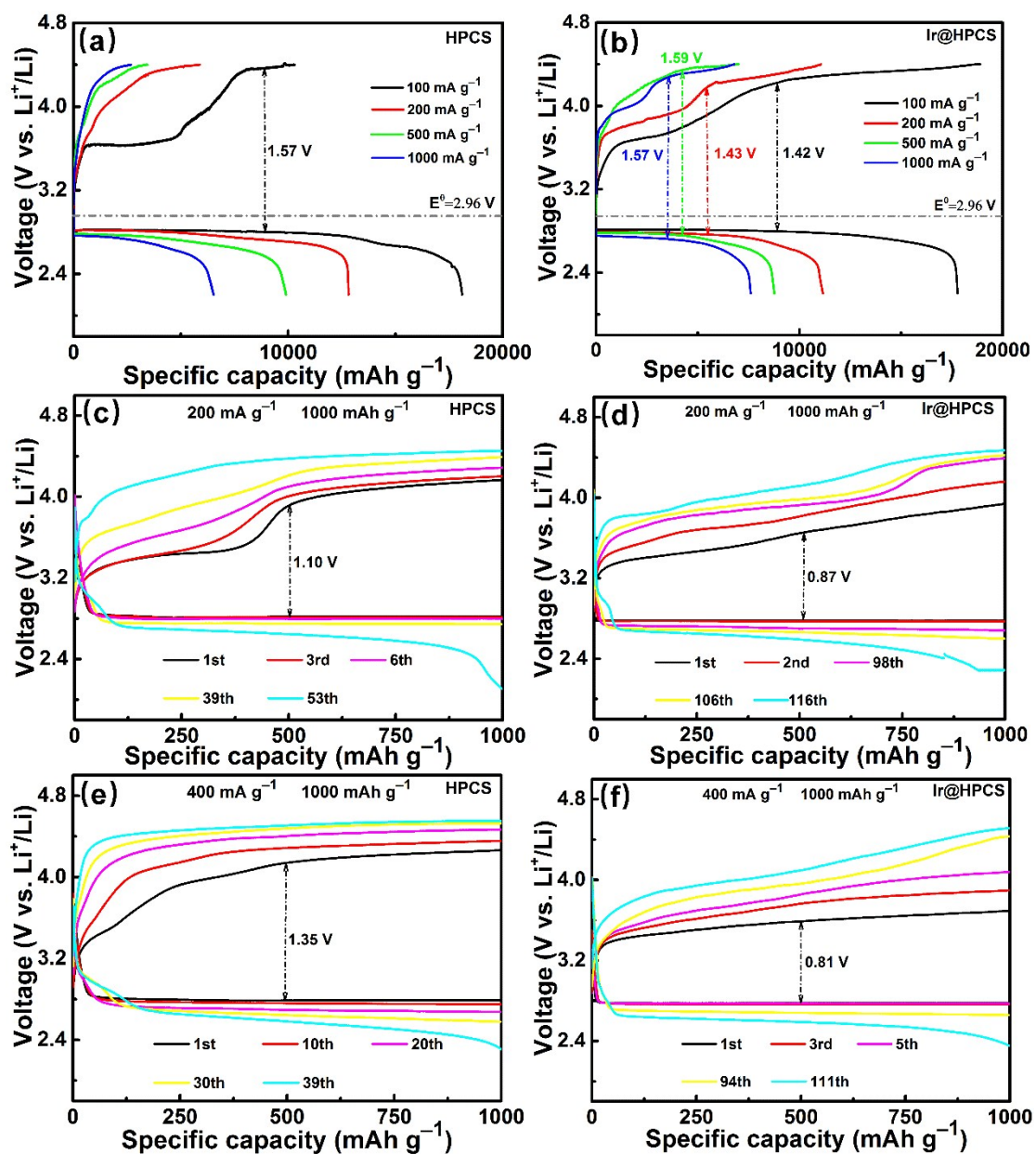
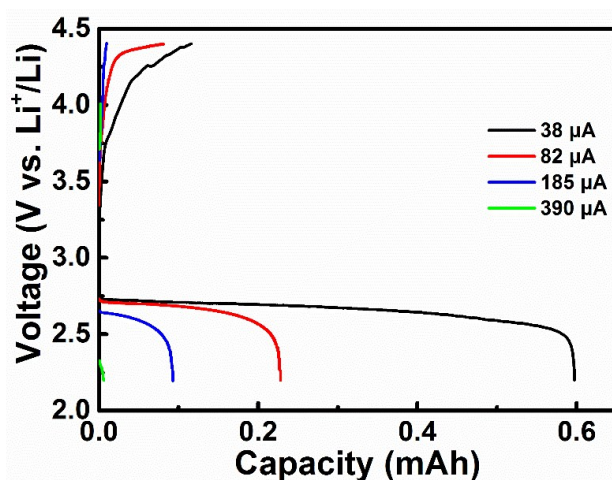


Fig. S11 (a) SEM image of the Super P electrode. (b) The  $N_2$ -adsorption/desorption isotherms and pore-size distribution plot (inset) of Super P.



**Fig. S12** The rate performance of LOBs with (a) HPCS and (b) Ir@HPCS cathodes within 2.2 to 4.4 V. The cyclic performance of LOBs with (c, e) HPCS and (d, f) Ir@HPCS cathodes at 200 and 400 mA g<sup>-1</sup> with a capacity restriction of 1000 mAh g<sup>-1</sup>.



**Fig. S13** Galvanostatic discharge/charge curves of pure carbon paper based cathodes at different current in the voltage range of 2.2–4.4 V.

In order to calculate the capacity contribution rate of carbon paper more accurately, we investigated the discharge/charge curves (Fig. S13) of pure carbon paper based electrode at the same current (absolute current value,  $\mu\text{A}_{\text{electrode}}$ ) as IrCo@HPCS based electrode in this paper. The calculated superficial discharge capacity contribution of carbon paper in IrCo@HPCS based cathode at 38, 82, 185, and 390  $\mu\text{A}$  are 8.9%, 4.3%, 2.4%, and 0.2%, respectively. For example, at 38  $\mu\text{A}$ , the superficial discharge capacity contribution rate is 8.9% ( $0.597 \text{ mAh} \div (17690 \text{ mAh g}^{-1} \times 0.38 \text{ mg}) = 8.9\%$ ). It can be seen that with the increase of current value, the superficial capacity contribution rate decreases significantly. Moreover, the carbon paper has a very weak OER activity and hardly promotes the decomposition of  $\text{Li}_2\text{O}_2$  [1], also as shown in Fig. S13 (the charge curves).

Furthermore, the discharge reaction in Li–O<sub>2</sub> battery mainly occurs at the three-phase interface of electrolyte/electrode/oxygen, and the solubility and conductivity of the formed  $\text{Li}_2\text{O}_2$  products are very poor [2–4]. It is very difficult for O<sub>2</sub> and Li<sup>+</sup> to

pass through the catalyst layer to reach the surface of the carbon paper for reaction.  $\text{Li}_2\text{O}_2$  is more easily formed on the surface of catalyst in kinetics. Therefore, it can be reasonably inferred that the real contribution capacity of pure carbon paper is much smaller than the measured value, although the actually exposed surface area of carbon paper cannot be measured by our current means.

Based on the above analysis, we think that carbon paper has little influence on the performance evaluation of our catalysts, because most of our tests were carried out at relatively high current density  $\geq 82 \mu\text{A}_{\text{electrode}}$  ( $\geq 200 \text{ mA g}^{-1}$  in our paper), and carbon paper had been uniformly covered with catalysts and it also had the same effect on all investigated catalysts. On the other hand, at very low current density, pure carbon paper may contribute a certain capacity, but due to the barrier of catalyst layer, its actual capacity contribution is difficult to evaluate. The capacity contribution of carbon paper collectors should be further studied in the future.

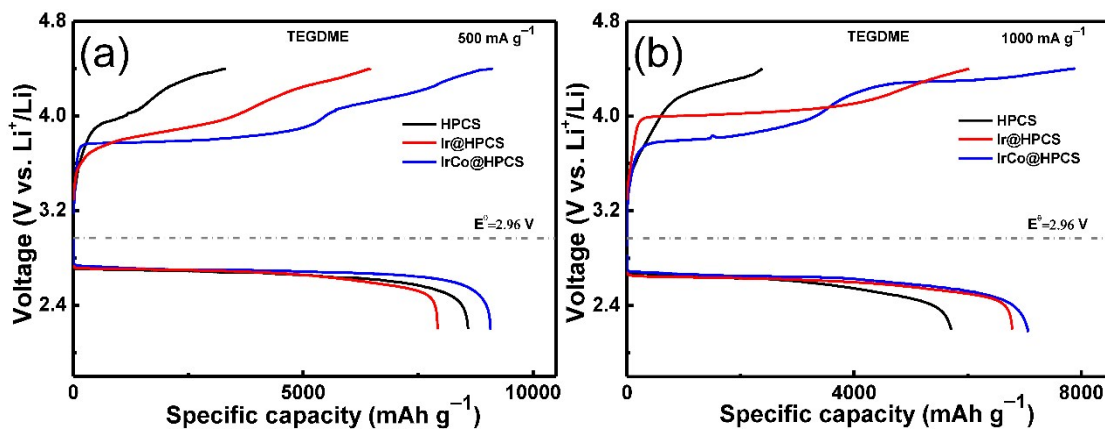


Fig. S14 Galvanostatic discharge/charge curves of HPCS, Ir@HPCS, and IrCo@HPCS based cathodes in 1 M LiTFSI/TEGDME electrolyte at (a) 500 mA g<sup>-1</sup> and (b) 1000 mA g<sup>-1</sup> within 2.2 to 4.4 V.

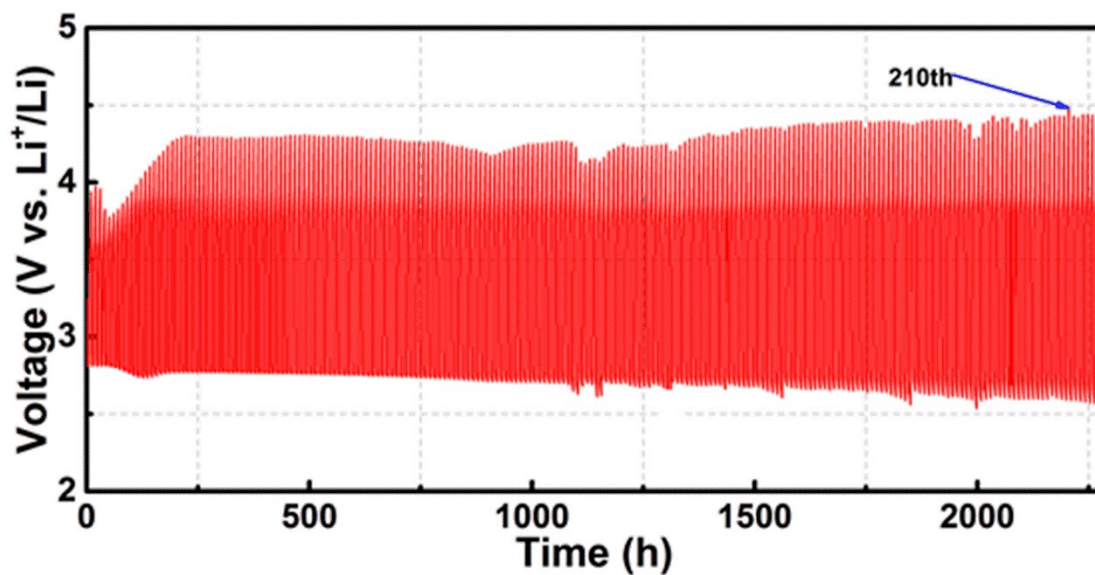


Fig. S15 Time-Voltage (T-V) curve of the IrCo@HPCS electrode with a capacity limitation of 1000 mAh g<sup>-1</sup> at a current density of 200 mA g<sup>-1</sup>.

**Table S4.** Summary of Li–O<sub>2</sub> batteries performances with carbon-based catalysts.

Catalysts	Discharge capacity (Current density)	Total overpotential (V)	Cycle numbers (Restricted capacity, Current density)	Ref.
Flexible bimodal porous CNT paper	5500 mAh g <sup>-1</sup> (500 mA g <sup>-1</sup> )	~1.7	~100 (1000 mAh g <sup>-1</sup> , 500 mA g <sup>-1</sup> )	[5]
Pd–flexible textile cathode	~8.6 mAh cm <sup>-2</sup> (0.1 mA cm <sup>-2</sup> )	~1.35	~50 (1.0 mAh cm <sup>-2</sup> , 0.1 mA cm <sup>-2</sup> )	[6]
Pt–hollow graphene nanocages	5600 mAh g <sup>-1</sup> (100 mA g <sup>-1</sup> )	~0.8	~54 (1000 mAh g <sup>-1</sup> , 100 mA g <sup>-1</sup> )	[7]
Ru–porous carbon skeleton	12400 mAh g <sup>-1</sup> (200 mA g <sup>-1</sup> )	~0.26	~100 (1000 mAh g <sup>-1</sup> , 400 mA g <sup>-1</sup> )	[8]
Ir@NHCSs	6573 mAh g <sup>-1</sup> (200 mA g <sup>-1</sup> )	~1.09	~83 (1000 mAh g <sup>-1</sup> , 400 mA g <sup>-1</sup> )	[9]
Free-standing PdNi–N, S– PC/CP	9965 mAh g <sup>-1</sup> (300 mA g <sup>-1</sup> )	~1.05	~67 (1000 mAh g <sup>-1</sup> , 300 mA g <sup>-1</sup> )	[10]
FeCo–CNTs	3600 mAh g <sup>-1</sup> (250 mA g <sup>-1</sup> )	~1.65	~50 (1000 mAh g <sup>-1</sup> , 100 mA g <sup>-1</sup> )	[11]
PdCuW–NS/C skeleton	5725 mAh g <sup>-1</sup> (300 mA g <sup>-1</sup> )	~1.6	~70 (500 mAh g <sup>-1</sup> , 300 mA g <sup>-1</sup> )	[12]
IrCo@HPCS skeleton	12996 mAh g <sup>-1</sup> (200 mA g <sup>-1</sup> )	~1.36	~210 (1000 mAh g <sup>-1</sup> , 200 mA g <sup>-1</sup> )	This work

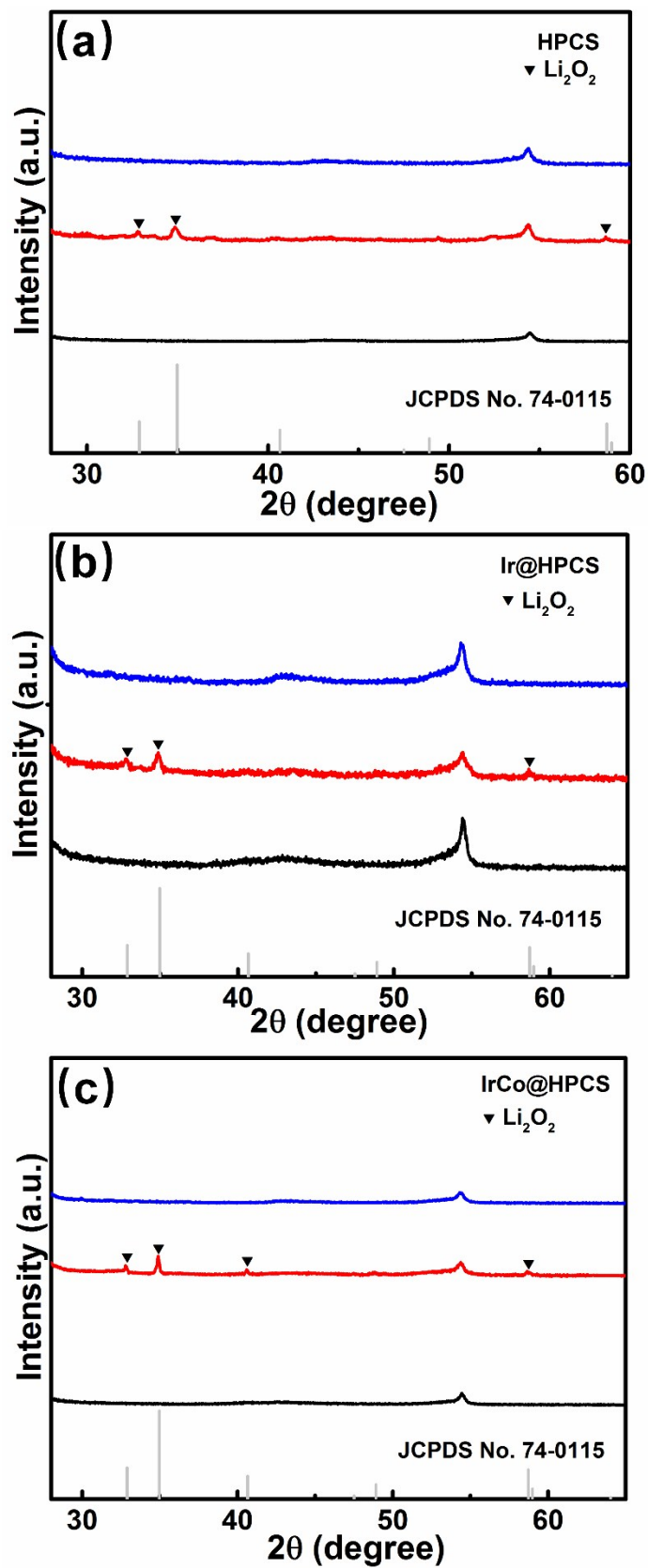
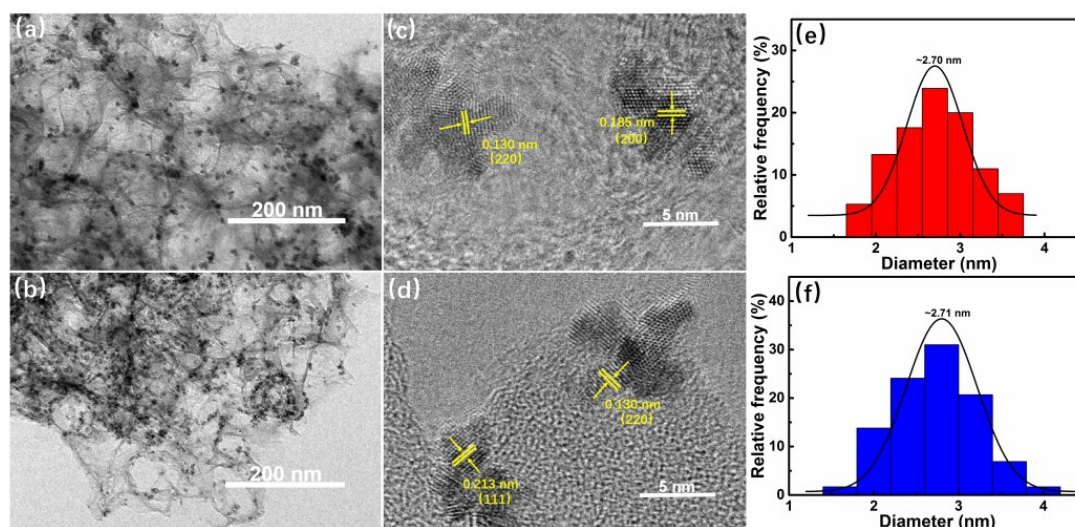
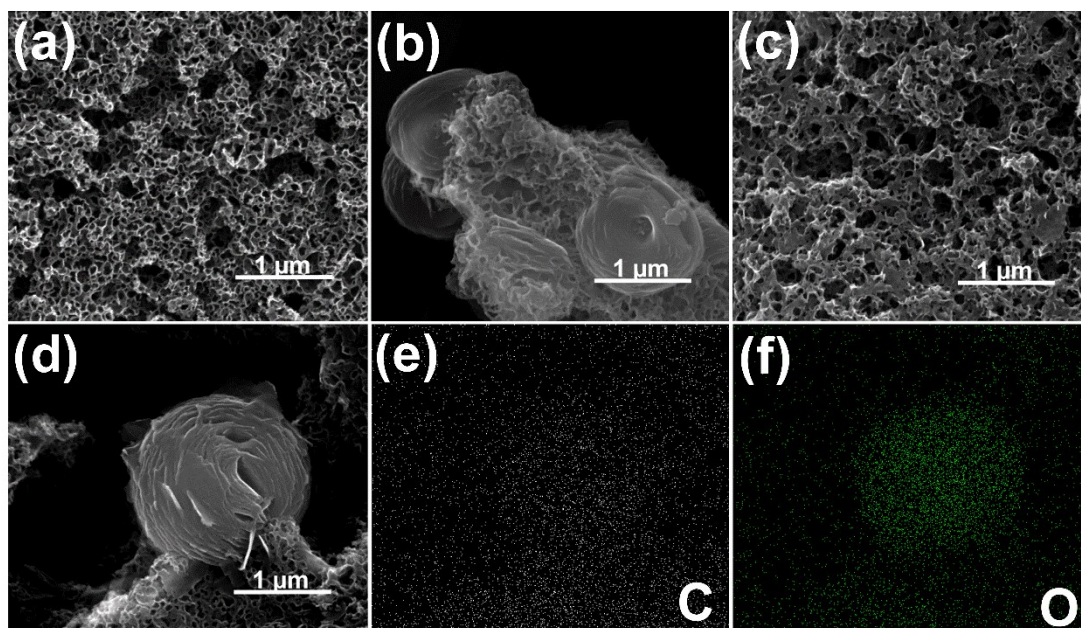


Fig. S16 XRD patterns of the pristine, after 1st discharge and recharge electrodes.



**Fig. S17** (a, b) TEM images, (c, d) HRTEM images, and (e, f) corresponding IrCo nanoparticles diameter distribution histograms of IrCo@HPCS based cathodes after (a, c, e) 50 and (b, d, f) 100 cycles under a limited capacity of  $1000 \text{ mAh g}^{-1}$  at  $200 \text{ mA g}^{-1}$ .

As can be seen in Fig. S17a and b, IrCo nanoparticles on HPCS maintained small particle size and uniform distribution with no obvious agglomeration after 50 or 100 cycles, confirming the good stability of the IrCo@HPCS catalyst. HRTEM patterns (Fig. S17c and d) clearly confirm the existence and crystallinity of IrCo bimetal. The diameter distribution histograms (Fig. S17e and f) show that the average particle size of IrCo nanoparticles after cycling is  $\sim 2.70 \text{ nm}$ , which is comparable to that of the pristine IrCo nanoparticles. The superior stability of IrCo@HPCS catalysts can be attributed to the strong physical and chemical interactions between IrCo nanoparticles and HPCS substrates. Moreover, the 3D cross-linked porous skeleton of HPCS, with good mechanical strength and large specific surface area, can effectively inhibit the agglomeration of IrCo nanoparticles [13].



**Fig. S18** SEM images of the HPCS cathodes: (a) pristine, (b) after the 1st discharge, and (c) after the 1st recharge. (d) The SEM images of toroid-shaped  $\text{Li}_2\text{O}_2$  in the HPCS cathode, and (e–f) the corresponding EDS mappings of (d).

## References

- [1] J. Wang, L. L. Liu, S. L. Chou, H. K. Liu and J. Z. Wang, *J. Mater. Chem. A*, 2017, **5**, 1462–1471.
- [2] J. Kang, Y. S. Jung, S.-H. Wei and A. C. Dillon, *Physical Review B*, 2012, **85**, 035210 (1–5).
- [3] Z. Y. Lyu, Y. Zhou, W. R. Dai, X. H. Cui, M. Lai, L. Wang, F. W. Huo, W. Huang, Z. Hu and W. Chen, *Chem. Soc. Rev.*, 2017, **46**, 6046–6072.
- [4] Y. F. Xu, Y. Chen, G. L. Xu, X. R. Zhang, Z. H. Chen, J. T. Li, L. Huang, K. Amine and S. G. Sun, *Nano Energy*, 2016, **28**, 63–70.
- [5] H. Lee, H. Kim, M. Kim, Y. Bae, W. Baek, Kwangjin Park, S. Park, T. Kim, H. Kwon, W. Choi, K. Kang, S. Kwon and D. Im, *Carbon*, 2017, **117**, 454–461.
- [6] S. M. Xu, Y. G. Yao, Y. Y. Guo, X. Q. Zeng, S. D. Lacey, H. Y. Song, C. J. Chen, Y. J. Li, J. Q. Dai, Y. B. Wang, Y. N. Chen, B. Y. Liu, K. Fu, K. Amine, J. Lu and L. B. Hu, *Adv. Mater.*, 2017, **30**, 1704907–1704914.

- [7] Y. Xing, F. Wu, X. Q. Zeng, Y. F. Yuan, X. Y. Zhang, R. S.-Yassar, J. G. Wen, L. Li, R. J. Chen, J. Lu and K. Amine, *Adv. Funct. Mater.*, 2016, **26**, 7626–7633.
- [8] B. Sun, X. Guo, J. Q. Zhang, H. Liu and G. X. Wang, *J. Mater. Chem. A*, 2016, **4**, 9774–9780.
- [9] W. Sun, J. R. Shen, H. T. Wu, J. S. Qiao, H. Q. Cai, Z. H. Wang and K. N. Sun, *Chem. Eng. J.*, 2019, **358**, 340–350.
- [10] X. Z. Ren, M. J. Huang, S. Luo, Y. L. Li, L. B. Deng, H. W. Mi, L. N. Sun and P. X. Zhang, *J. Mater. Chem. A*, 2018, **6**, 10856–10867.
- [11] T.-G. Kang, W.-J. Kwak, Y.-K. Sun and Y. J. Lee, *J. Mater. Chem. A*, 2016, **4**, 7020–7026.
- [12] S. Lin, Y. L. Li, S. Luo, X. Z. Ren, L. B. Deng, H. W. Mi, P. X. Zhang, L. N. Sun and Y. Gao, *Electrochimica Acta*, 2018, **272**, 33–43.
- [13] X. Y. Lu, X. L. Sun, S. Kaskel and O. G. Schmidt, *J. Mater. Chem. A*, 2017, **5**, 6284–6291.